



Article

Degradation Evaluation of Lithium-Ion Batteries in Plug-In Hybrid Electric Vehicles: An Empirical Calibration

Hongchang Cai ^{1,†}, Xu Hao ^{2,†} , Yong Jiang ², Yanan Wang ^{3,*} , Xuebing Han ³, Yuebo Yuan ³, Yuejiu Zheng ^{1,*}, Hewu Wang ³ and Minggao Ouyang ³

¹ College of Mechanical Engineering, University of Shanghai for Science and Technology, Shanghai 200093, China

² School of Mechanical Engineering, University of Science and Technology Beijing, Beijing 100083, China

³ State Key Laboratory of Automotive Safety and Energy, Tsinghua University, Beijing 100084, China

* Correspondence: wangyn7@mail.tsinghua.edu.cn (Y.W.); yuejiu.zheng@usst.edu.cn (Y.Z.)

† These authors contributed equally to this work.

Abstract: Battery life management is critical for plug-in hybrid electric vehicles (PHEVs) to prevent dangerous situations such as overcharging and over-discharging, which could cause thermal runaway. PHEVs have more complex operating conditions than EVs due to their dual energy sources. Therefore, the SOH estimation for PHEV vehicles needs to consider the specific operating characteristics of the PHEV and make calibrations accordingly. Firstly, we estimated the initial SOH by combining data-driven and empirical models. The data-driven method used was the incremental state of charge (SOC)-capacity method, and the empirical model was the Arrhenius model. This method can obtain the battery degradation trend and predict the SOH well in realistic applications. Then, according to the multiple characteristics of PHEV, we conducted a correlation analysis and selected the UF as the calibration factor because the UF has the highest correlation with SOH. Finally, we calibrated the parameters of the Arrhenius model using the UF in a fuzzy logic way, so that the calibrated fitting degradation trends could be closer to the true SOH. The proposed calibration method was verified by a PHEV dataset that included 11 vehicles. The experiment results show that the root mean square error (RMSE) of the SOH fitting after UF calibration can be decreased by 0.2–14% and that the coefficient of determination (R^2) for the calibrated fitting trends can be improved by 0.5–32%. This provides more reliable guidance for the safe management and operation of PHEV batteries.



Citation: Cai, H.; Hao, X.; Jiang, Y.; Wang, Y.; Han, X.; Yuan, Y.; Zheng, Y.; Wang, H.; Ouyang, M. Degradation Evaluation of Lithium-Ion Batteries in Plug-In Hybrid Electric Vehicles: An Empirical Calibration. *Batteries* **2023**, *9*, 321. <https://doi.org/10.3390/batteries9060321>

Academic Editor: Wilhelm Pfleging

Received: 7 May 2023

Revised: 28 May 2023

Accepted: 5 June 2023

Published: 10 June 2023



Copyright: © 2023 by the authors. Licensee MDPI, Basel, Switzerland. This article is an open access article distributed under the terms and conditions of the Creative Commons Attribution (CC BY) license (<https://creativecommons.org/licenses/by/4.0/>).

1. Introduction

Plug-in electric vehicles (PEVs) have reached new sales worldwide despite the COVID-19 pandemic and supply chain challenges. Among these vehicles, the plug-in hybrid electric vehicle (PHEV) is welcomed by consumers because it is free of the challenges of range anxiety and charging infrastructure construction difficulty. Sales of PEVs doubled in 2021 from the previous year to a new record of 6.6 million. About 1.9 million new plug-in hybrid electric vehicles were sold worldwide in 2021. In 2021, nearly 30% of electric vehicle sales were attributed to plug-in hybrid electric vehicles (PHEVs), indicating its acceptance by different countries [1,2]. In the largest PEV market, China, PHEV sales numbered 148,000 in 2022, accounting for 22.8% of the light-duty vehicle sector, which was due to the battery electric vehicle (BEV)-favored policy in effect in China. PHEVs have two kinds of onboard energy storage, the electricity stored in the battery and the chemical energy stored in the fuel (e.g., gasoline, diesel), which drive its operation either alone or simultaneously; therefore, it can help consumers free themselves from the challenges of range anxiety and charging infrastructure construction difficulty. According to a consumer survey in China, over 50% of consumers accept PHEVs [3,4]. However, the battery durability of PHEVs has become the bottleneck of PHEV promotion. Currently, the lifespan of lithium-ion batteries

in different material systems ranges from 500 to 2500 complete charge–discharge cycles [5]. However, there is still a strong demand from consumers for lithium-ion batteries to have even greater durability, as this can lead to better stability and economy [6]. Fundamentally, battery lifespan extension requires breakthroughs in the materials used for lithium-ion batteries [5,7,8]. For the battery management aspect, reasonable lifespan estimation, prediction, and control can also contribute to the reduction of battery degradation during actual vehicle operation, thus extending battery lifespan [9–13].

The state of health (SOH) is defined to quantify a battery’s durability and lifespan [14]. There has been plenty of battery SOH research. For instance, Berecibar et al. [15,16] applied differential voltages for capacity estimation, which requires obtaining the differential voltage curve under a small constant current charging condition. Similarly, Li et al. [17–19] applied incremental capacity curves for capacity estimation, which also require constant current charging conditions. Both methods, while having high estimation accuracy, are limited by complex actual vehicle operating conditions and are hence hard to apply to reality. Some researchers have also used machine learning algorithms for capacity estimation. For example, Zhu et al. [20] used the relaxation voltage as a feature and achieved an accurate capacity estimation by using support vector regression algorithms. However, obtaining the relaxation voltage requires long-term rest, so it is also limited by the actual vehicle conditions. Qian et al. [21–23] used a convolutional neural network to effectively estimate the capacity using random charging segments. The most common method is the incremental state of charge (SOC)-capacity method [24]; this method is easy to implement and is more suitable for actual driving conditions, but its estimation accuracy is limited by the SOC range and current sampling accuracy. Some researchers have also used the open-loop Arrhenius model to estimate the SOH. Although the Arrhenius model can be applied to any operating condition, it is prone to parameter mismatching during battery aging. Thus, to address the problem of the Arrhenius model, Zheng et al. [25] estimated the capacity based on the fractional charge curve and calibrated the Arrhenius model parameters using the sequential extended Kalman filter algorithm. Finally, the two methods were fused to achieve an accurate capacity estimation.

Despite the limited precision of the incremental SOC-capacity method that is attributable to the restricted range of SOC values, the temporal dynamics of this approach conform to the underlying aging patterns of batteries. Consequently, by leveraging the incremental SOC-capacity method to derive the battery capacity and by subsequently fitting an Arrhenius model, it becomes feasible to perform an SOH estimation that mitigates parameter mismatching issues [26]. However, the above methods are often applied to BEVs; there is still a research gap for PHEV SOH research, which is mainly due to the lack of empirical data.

In the charging mode, both PHEVs and BEVs have the capability of fast charging and slow charging [27]. In the discharge mode, BEVs are solely electric-driven, whereas PHEVs can adopt two types of onboard energy storage—the electricity stored in the battery, as well as the chemical energy stored in fuels such as gasoline or diesel—to power its operation either independently or simultaneously [28,29]. Based on this most essential difference, and when compared with BEVs, PHEVs have many factors to be considered in the lifetime estimation that are not necessary for BEVs. The main factors related to PHEV battery lifetime may include pure electric driving range, average daily vehicle kilometers, vehicle kilometers travelled during two charging sessions (CVKT), electric-driven vehicle kilometers travelled during two charging sessions (E-CVKT), utility factor (UF) [30], and so on. Among them, the UF [31] is usually adopted by PHEVs to evaluate the distance ratio that is driven by electricity, perhaps because it is the most distinct feature between PHEV and BEV. The complexity of the energy sources makes it difficult to directly evaluate the distance driven by electricity as well as the condition of battery; therefore, its impact on PHEV battery SOH remains uncertain. Hence, this work attempts to identify the influence of these factors on PHEV battery lifetime, then take the factor influence into consideration for battery SOH prediction.

The first and main contribution of this work is the calibration of the traditional SOH Arrhenius equation to better fit PHEVs, including their driving patterns, in the calculation. Correlations among several factors of battery SOH were also investigated, and the main factor was selected for the calibration of the SOH Arrhenius equation. The calibration was based on the empirical driving data of the PHEV, which is another contribution of this work. The research on the battery SOH of PHEVs will help optimize the battery capacity and size from the durability perspective for auto companies; it will also guide users to drive the vehicle in a better way to extend the battery life. The main research content and structure of this paper are as follows. Section 2 introduces the capacity estimation method and empirical dataset. Section 3 introduces the SOH calibration method and calibration results; lastly, the summary and discussion are provided.

2. Method and Dataset

2.1. PHEV Data Description

Considering the complexity of PHEV energy sources, actual driving data are needed to investigate the battery degradation of PHEVs. Therefore, we conducted the SOH calculation using empirical data obtained from real-world PHEV driving scenarios. The actual driving data were directly collected from the onboard system from the original equipment manufacturer (OEM) data platform. The data collected from the OEM's platform adheres to the GB/T 32960.3-2016 standard [32]. The dataset includes eight distinct data fields, which are summarized in Table 1.

Table 1. Data introduction.

Data	Meaning and Provisions
Battery charge status	1—Parking charge; 2—Driving charge; 3—Uncharged
Total odometer	Vehicle's total mileage (km)
Speed	Speed of a vehicle (km/h)
SOC	State of charge
Terminal time	Running time
Vehicle operation state	The type of power used to propel the vehicle during operation: 1—Pure electric; 2—Hybrid electric; 3—Oil fuel
Total voltage	Battery voltage (V)
Total current	Battery current (A)

In order to specifically analyze the battery degradation of PHEVs while mitigating the influence of other factors such as temperature, we selected vehicles from the same compact brand and model that have been in operation in the same city for over 6 months from the platform. Therefore, a total of 11 vehicles running in Chongqing, China, were chosen, providing a dataset of 13,590 km for the calculation. The PHEVs are geographically located between 28°10'–32°13' N and 105°11'–110°11' E, as depicted in Figure 1.

The selected vehicle is a domestically manufactured compact PHEV model equipped with a 1.5 T engine and 220 kW motor. In accordance with the New European Driving Cycle (NEDC), the fuel consumption of this vehicle is recorded as 1.6 L per 100 km. The battery system installed in this PHEV consists of a 12.96 kWh lithium nickel manganese cobalt (NMC) cathode battery, which enables an all-electric range of 60 km. Regarding the NMC battery, the battery pack structure is denoted as 1P96S, indicating a configuration of 1 cell in parallel and 96 cells in series. The battery has a capacity of 37 Ah, rated voltage of 350 V, and peak power of 120 kW. These specifications contribute to the performance and capabilities of the PHEV, allowing for efficient and reliable electric propulsion.



Figure 1. Data distribution.

The data processing included data cleaning, segmentation, and data storage into a designated dataset, which was categorized according to individual trips. In this work, the date was recorded every 10 s. Note that this 10-s interval is not a definite standard. As vehicles drive in Chongqing, a city with tall buildings and a high housing density, data transmission between the vehicle terminal and the data collection platform may be blocked, resulting in data loss. To ensure data accuracy and reliability, it was imperative to preprocess the raw data using the environment of MATLAB (ver. R2020b) by Mathworks®. Data processing included the following three steps [4]:

(1) Data cleaning

Missing data points may occur due to various reasons, such as the obstructions of buildings in the cities or tunnels or other network issues. These missing points can be rectified through smoothing techniques.

(2) Trips segmentation

Any two adjacent data points were divided into two segments if the time interval between them was longer than 30 min. The segment of charge status = 1 was defined as the parking charging segment, and the parking charging segment with constant mileage was merged into one segment because of the data losses. After that, the segment between two parking charging segments was the driving segment.

(3) Outlier trip deletion

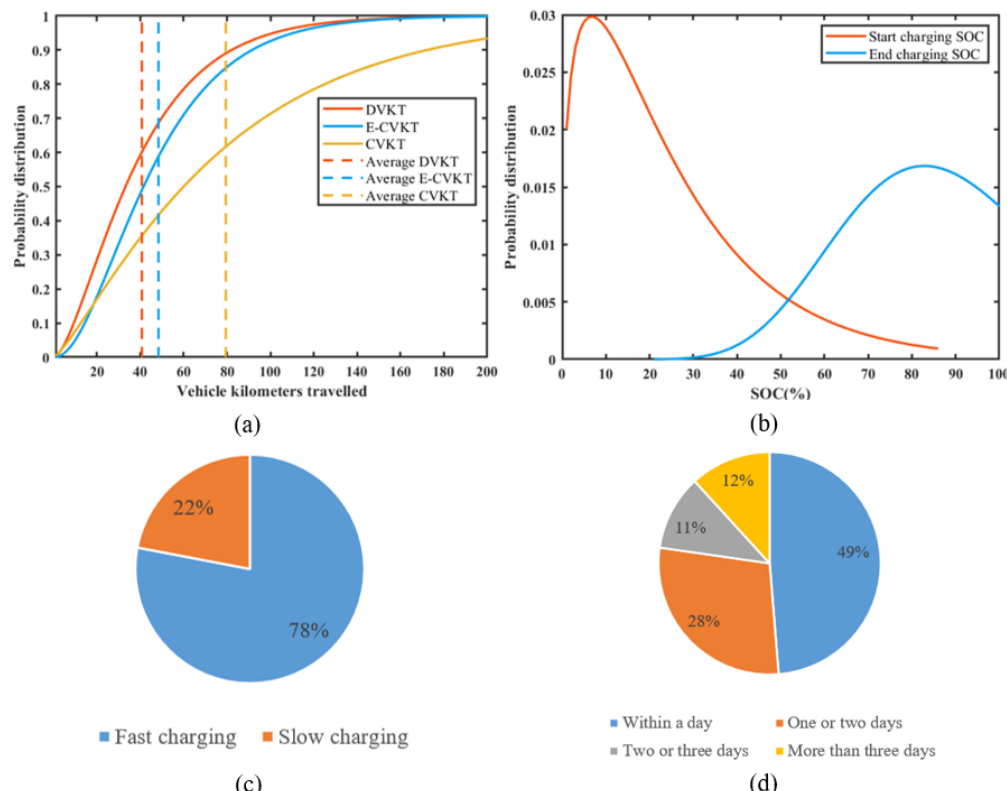
In this step, the data was further filtered on a trip-by-trip basis. To strike a balance between preventing data drift and including as much of the available data as possible, trips lasting less than 5 min or 1 km were excluded to avoid possible deviations in the data.

After the data processing, the single-charging event data and the travel data between two charging sessions were extracted. Based on these segments, the data for 11 vehicles were calculated, such as the total mileage, average daily vehicle kilometers travelled (DVKT), and UF, as shown in Table 2.

Table 2. Data summary.

Data	Description
Number of vehicles	11
Total mileage	13,590 km
Average driving days	233
Average DVKT	41 km
Average utility factor	0.87
Average start charging SOC	22%
Average end charging SOC	86%
Percentage of miles traveled above 60 km/h	22%

The travel and charging pattern of the PHEVs are primarily summarized in Figure 2. The average daily vehicle kilometers traveled (DVKT) for the PHEVs was recorded as 41 km. Additionally, the CVKT was 79 km, with 48 km being attributed to electric driving (E-CVKT). Based on the theoretical all-electric range of 60 km, it can be inferred that approximately 59% of the PHEV's driving mileage was powered by electricity, as depicted in Figure 2a. The average start charging SOC was 22%, while the average end charging SOC was 86%. As shown in Figure 2b, the PHEVs started charging when the battery was 0–20% (at a low level) and ended charging when the battery was 80–100% (at a high level). These PHEVs can be charged at up to 3.5 kW (slow charging) and 7 kW (fast charging). Compared with slow charging, PHEVs used fast charging more, and their ratio reached 78%, as shown in Figure 2c. The charging frequency, which was defined according to the charging sessions gap, is quantified in Figure 2d. From the charging frequency, the PHEVs were basically charging once within two days. The proportion that were charging once a day (gap between two adjacent charging sessions was less than 24 h) was 49%, and the number charging once within two days (gap between two adjacent charging sessions was less than 48 h) reached 77%.

**Figure 2.** Travel pattern: (a) vehicle kilometers travelled (VKT), (b) charging start and end SOC, (c) charging preference, (d) charging frequency.

To further illustrate the ratio of electric distance in this PHEV SOH research study, the utility factor, which is intuitively defined by dividing the electric driving range (typically the charging depleting range or CD range) by the total distance traveled was adopted. The UF was primarily defined by Society of Automotive Engineers (SAE); it can be calculated by summing the minimum value between the charging depleting (CD) range (D) and daily travel distance (d_k) and then dividing the value by the sum of all distances traveled [33]:

$$\text{UF}(D) = \frac{\sum_{d_k} \min(d_k, D)}{\sum_{d_k} d_k} \quad (1)$$

The UF can be directly referred to from the travel data, as the power to drive the vehicle at each moment is offered. A simplified way of understanding the UF is as the ratio of the CD range to the total distance traveled. The distribution and average of the UF are summarized and presented in Figure 3. Specifically, for the PHEVs with a 60-km all-electric range in the analyzed case, approximately 42% of the trips exhibited a UF in the range of 0.9–1.0. Moreover, over 87% of the trips had a UF exceeding 0.5, as depicted in Figure 3a. From the average vehicle UF perspective, as shown in Figure 3b, the average UF for each vehicle was above 0.5. Notably, 82% of the PHEVs in this dataset demonstrated an average UF exceeding 0.7. This indicates that, in most trips, the proportion of mileage driven using electricity was significantly higher compared with that driven using gasoline.

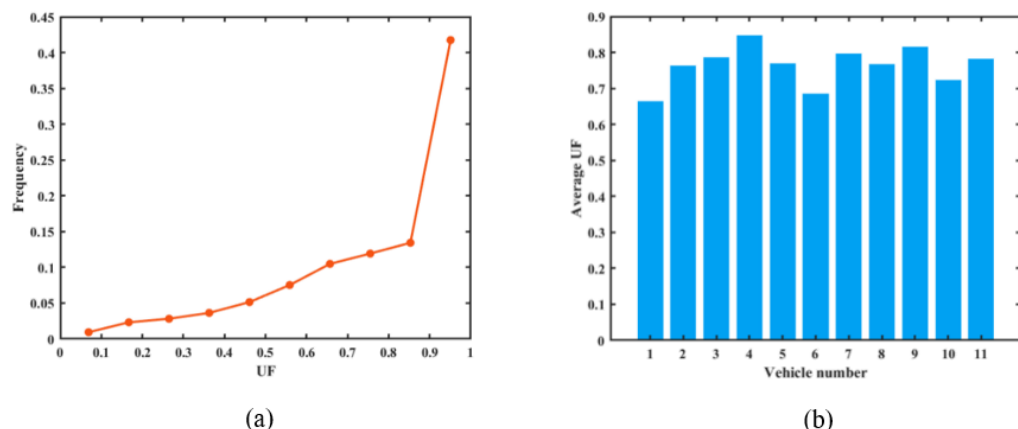


Figure 3. (a) UF distribution frequency of all PHEVs; (b) average UF for each PHEV in the empirical case.

In order to study the attenuation rules of the PHEV battery capacity, we needed to process the charging segment data to obtain the fitting trends of the SOH, and we also needed to obtain the variation of battery SOH. The calculation process of the SOH included the following steps:

(1) Discrete calculation of SOH

According to the charging snippets obtained from the vehicle, the ampere-hour integral between two points was divided by the difference value of its corresponding SOC to obtain the capacity in every snippet. The least square method was added to achieve a set of discrete SOH points, with $\text{SOH} \geq 100$ being deleted.

(2) Fitting trends of SOH

The SOH estimation was modified using Kalman filtering and fuzzy logic, and it was fitted using an Arrhenius model to obtain the SOH fitting trends. The fitting curves of SOH are shown in Figure 4. From the curves, the SOH fitting curves of two vehicles were lower than the 80% level, while the SOH fitting curves of seven vehicles were higher than the 90% level. Hence, the battery health level of these two vehicles was significantly lower than that of the other vehicles.

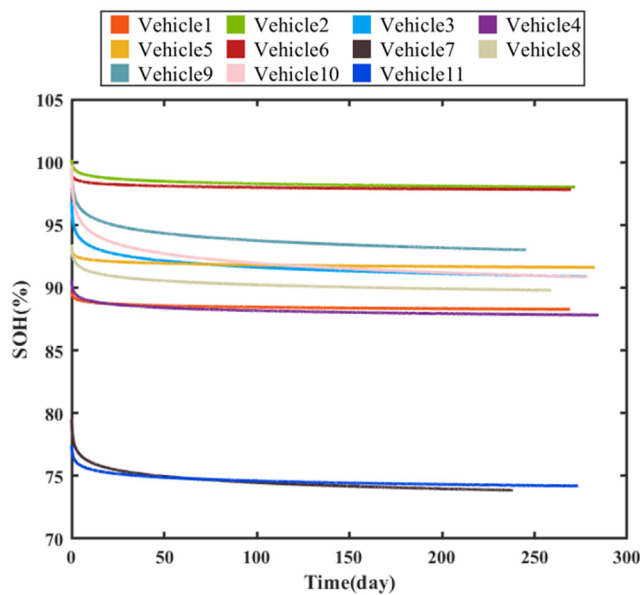


Figure 4. SOH fitting curves based on 11 PHEVs in the empirical case.

2.2. Correlation Analysis between Each Travel Feature

This work attempted to find out which features have an effect on SOH attenuation. According to the divided parking charging segment and driving segment, the following vehicle features can be extracted: the start charging SOC, charging duration, percentage of miles traveled above 60 km/h (PTA60), rate of charge, rate of discharge, DVKT, E-CVKT, UF, and depth of charge (DOC); DOC is the range of SOC change during charging. Starting from the position where the slope of the SOH fitting curves gently changes, the real-time estimation of SOH was shred with 30 days as a unit, and the mean value of all travel features and SOH difference in each unit were calculated to find out the possible parameters that could be adopted to calibrate the SOH calculation, as shown in Table 3. In general, the correlation between the travel features and SOH difference were relatively low. Among them, the correlation coefficients between the UF and SOH difference were 0.41 and 0.31, respectively, which were higher than the others. The correlation coefficient of 0.41 between the UF and SOH difference indicated a moderate correlation between them. On the other hand, the correlation coefficient between the charging duration and SOH difference was 0.06, which was very low and suggested no significant correlation between them.

Table 3. Correlation analysis between SOH difference and each travel feature.

	Start Charging SOC	Charging Duration (h)	PTA60	Charging Rate	Discharging Rate	DVKT (km)	E-CVKT (km)	UF	DOC
Correlation coefficients	-0.19	0.06	-0.22	-0.16	-0.17	0.13	-0.19	0.41	0.31

To examine the correlation among different parameters, we utilized the Pearson correlation coefficient to assess the linear correlation between various travel pattern parameters/features. Based on the findings presented in Figure 5, the correlation coefficient between the UF and other variables was relatively low, indicating weak or even no correlation. As the ampere-hour integral of the SOH estimation reflects the DOC, we did not specifically discuss the correlation between the DOC and SOH difference. Instead, we focused on analyzing the impact of the UF on the SOH.

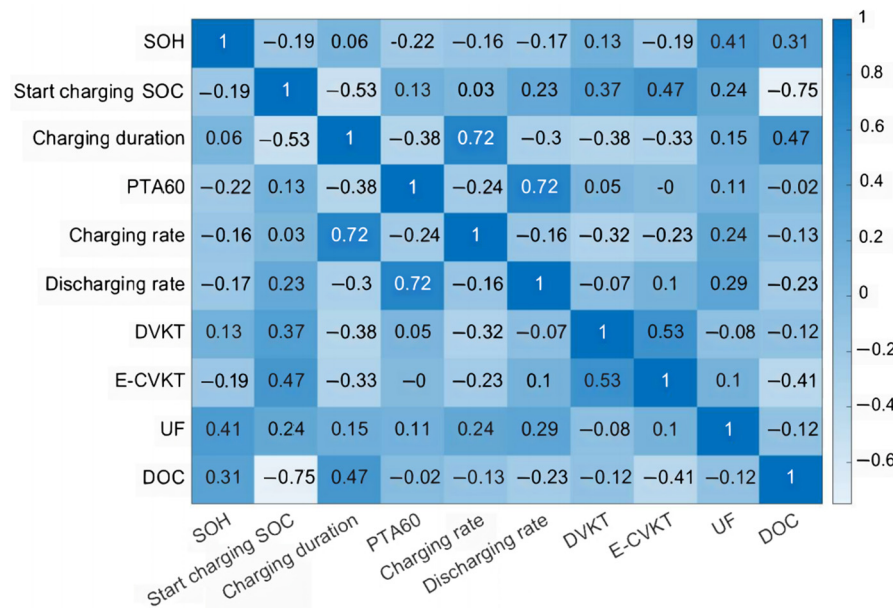


Figure 5. Correlation analysis: Pearson correlation among different travel pattern parameters.

2.3. SOH Prediction of PHEVs

2.3.1. Degradation Calculation

(1) SOH estimation

The SOH quantifies the health status of a battery, ranging from a fresh battery to a battery with degradation, up until battery retirement. The quantification of the SOH can be represented by either the battery capacity or internal resistance. In this study, the SOH was calculated based on the battery capacity, as shown in Equation (2) [26].

$$\text{SOH} = \frac{Q_\alpha}{Q_{\text{rate}}} \times 100\% \quad (2)$$

where Q_α is the available capacity, Q_{rate} is the battery rated capacity, and SOH is the ratio of available capacity Q_α and rated capacity Q_{rate} . An accurate determination of the battery capacity is crucial for obtaining precise SOH measurements. The accumulated state of charge (SOC)-capacity method, which utilizes battery charge and SOC, can be employed for battery capacity estimation. The accumulated charge, denoted as ΔAh , is obtained through the ampere integral method (Ah method). The capacity is then derived by dividing the accumulated charge ΔAh by the variation in the SOC (ΔSOC) [34]:

$$Q_{\alpha,\beta} = \frac{\Delta Ah}{\Delta \text{SOC}} = \frac{\int_{t_\alpha}^{t_\beta} I(\tau) d\tau}{\text{SOC}(t_\beta) - \text{SOC}(t_\alpha)} \quad (3)$$

where $Q_{\alpha,\beta}$ is the battery capacity, t_α and t_β are the start time and end time of a period of time $[t_\alpha, t_\beta]$, and $I(\tau)$ is the battery input current. The C-rate means the charging/discharging current speed to its rated capacity in an hour. From Equation (3), the Ah method and SOC are key for the estimation accuracy of the capacity. Moreover, the battery working temperature T can also affect the battery charging process and estimation accuracy. Hence, capacity $Q_{\text{temp_corr}}(T)$ with temperature calibration [26] is also applied as

$$Q_{\text{temp_corr}}(T) = Q_{\alpha,\beta} \times \left(1 - 2 \cdot 10^{-3} \times (T - 25^\circ)\right) \quad (4)$$

(2) Degradation prediction

Battery health and degradation can be predicted by applying the Arrhenius empirical aging model with the battery capacity estimated values. In general, the Arrhenius

empirical aging model is applied to calculate the real-time capacity loss [34], which can be presented as

$$Q_{\text{loss}} = Ae^{-\frac{E_a}{RT}} \cdot n^z \quad (5)$$

where Q_{loss} is the capacity loss in n cycles, A is the coefficient for exponential function, E_a is the activation energy, R is the gas constant, T is the operation temperature, and z is the exponent. Because the capacity is already calibrated by the temperature equation in Equation (4) to 25 °, the influence of temperature can be ignored in Equation (5). Hence, the Arrhenius empirical aging model in Equation (5) can be simplified as

$$Q_{\text{loss}} = \eta \cdot n^z \quad (6)$$

where η is a constant coefficient, and n is the time or cycle. It should be noted that n can also be expressed as mileage, which corresponds to only battery cycling life. If n is the time or cycle, it not only considers battery cycling life but also battery calendar life. In this work, n was presented as cycles. As for the degradation index z , it was always set as a constant for degradation ratio, which was considered as unchanging with time. Especially, for battery degradation that is mainly caused by solid electrolyte interphase (SEI), z is usually set as 1/2. However, in this work, the degradation index z was corrected by the UF to achieve a more accurate battery degradation prediction for the PHEVs.

2.3.2. Degradation Calibration with PHEV Pattern

(1) Discrete Arrhenius model

From the previous analysis, the UF acts as a key factor influencing the battery life of the PHEVs. In this work, we propose a UF correction to the Arrhenius aging model for a better prediction of battery life. As presented in Section 2.3.1, the Arrhenius empirical aging model (Equation (5)) has limitations when applied to dynamic operating conditions involving changing currents or varying temperatures. Hence, our research group has proposed a discrete aging model called the discrete Arrhenius aging model (DAAM) [35]. For the Arrhenius empirical aging model in Equation (6), the derivation of Equation (6) with cycle n can be presented as

$$\frac{dQ_{\text{loss}}}{dt} = z \cdot \eta \cdot n^{z-1} = z \cdot \eta \cdot \left(\frac{Q_{\text{loss}}}{\eta} \right)^{\frac{z-1}{z}} = z \cdot Q_{\text{loss}}^{\frac{z-1}{z}} \cdot \eta^{\frac{1}{z}} \quad (7)$$

Hence, the corresponding DAAM is presented as

$$Q_{\text{loss},n} = Q_{\text{loss},n-1} + z \cdot Q_{\text{loss},n-1}^{\frac{z-1}{z}} \cdot \eta^{\frac{1}{z}} \quad (8)$$

where $Q_{\text{loss},n}$ is the capacity loss after n battery cycles, $Q_{\text{loss},n-1}$ is the capacity loss after $(n - 1)$ battery cycles, and η is a pre-set constant in Equation (6). According to Equation (8), the capacity loss can be calculated for each cycle considering that the battery's operating conditions may change over time, as depicted in Figure 6. Assuming that a battery undergoes two primary operation conditions, ranging from being fresh to aging (condition1 and condition2 in Figure 6), the battery's aging trajectory may transition between these two conditions, resulting in the observed degradation curve illustrated in Figure 6. In conjunction with the previous analysis, the battery lifetime of the PHEVs is influenced by the UF. Therefore, the UF can be regarded as a dynamic condition within Figure 6. To account for the impact of the UF, the degradation index z in Equation (7) was adjusted by the UF.

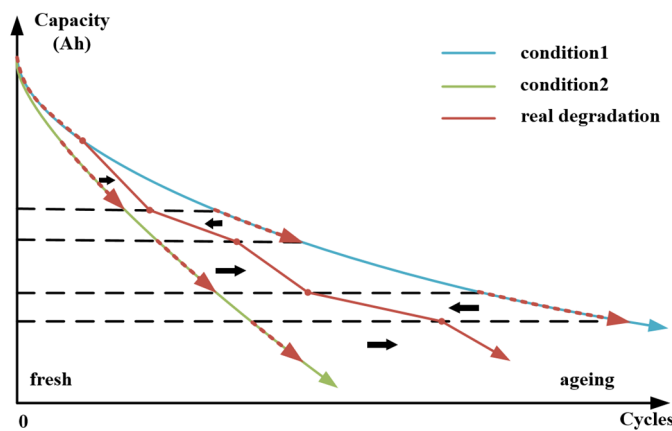


Figure 6. Schematic diagram of discrete Arrhenius model under various UF conditions. The two conditions (condition1 and condition2) illustrate two different operation conditions to present the dynamic working situations of the battery in PHEVs. The real degradation illustrates the real degradation trajectory from a fresh battery to an ageing battery.

(2) Calibration by UF

For the degradation index z correction of DAAM, a specific relationship between the UF and z would be constructed. Combined with fuzzy logic method [26], the calibration approach was proposed as

$$z_{\text{new}} = z + z \times (\text{UF} - \text{UF}_0) \quad (9)$$

where z_{new} is the corrected degradation index, UF is the averaged UF value calculated by a certain period, and UF_0 is the threshold value for UF to influence the battery degradation in a fuzzy logic. With the threshold UF_0 in Equation (9), the capacity loss and degradation trajectory would be calibrated by the UF in a fuzzy logic way; thus, the DAAM with corrected degradation index z_{new} can be presented as

$$Q_{\text{loss},n} = Q_{\text{loss},n-1} + z_{\text{new}} \cdot Q_{\text{loss},n-1}^{\frac{z_{\text{new}}-1}{z_{\text{new}}-1}} \cdot \eta^{\frac{1}{z_{\text{new}}}} \quad (10)$$

Combining Equation (9) and (10), if $\text{UF} > \text{UF}_0$, the degradation index z increases and the battery aging ratio is enlarged by UF, thus causing the capacity loss to be enlarged to achieve more serious battery degradation. In contrast, if $\text{UF} < \text{UF}_0$, the degradation index z decreases and the capacity loss is relieved to achieve slower battery degradation. In this way, with the UF changing in various cycles, the battery degradation is calibrated by different UF operation conditions. To illustrate the calibration effects, Figure 7 is provided. Figure 7a presents the schematic diagram of the UF calibration effects on the Arrhenius curve. Because a threshold UF_0 during UF changing needed to be pre-determined for accelerating degradation, a fuzzy logic in a certain UF range was applied. Figure 7b presents the working details of the UF calibration in a fuzzy logic way. To showcase the practical calibration effects on PHEVs, an example is presented in Figure 8. A PHEV from our dataset, which was introduced in Section 2.1, was selected to calculate the discrete Arrhenius curves through the proposed UF calibration method.

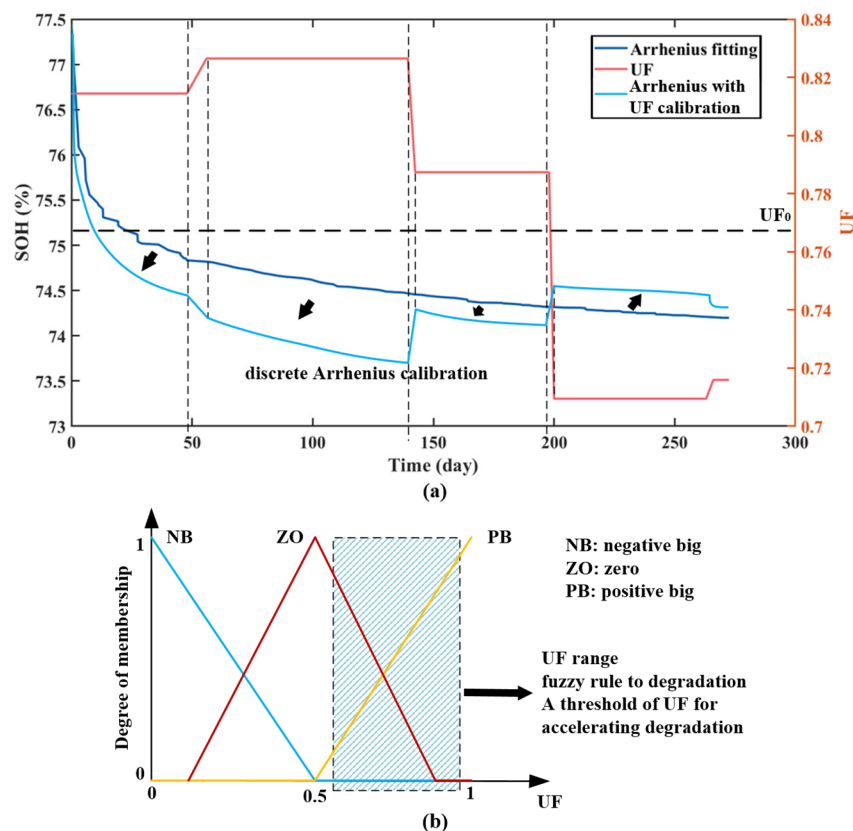


Figure 7. The proposed UF calibration method for battery degradation in a fuzzy logic way. **(a)** The schematic diagram to illustrate the calibration effects of the UF on an Arrhenius curve. Using a dynamic UF (the red curve) during battery lifetime, the Arrhenius fitting (the blue curve) was calibrated into a discrete Arrhenius curve (the light blue curve). **(b)** The fuzzy logic way of UF calibration. The UF calibrates battery degradation in a fuzzy rule in a certain UF range (the dashed box).

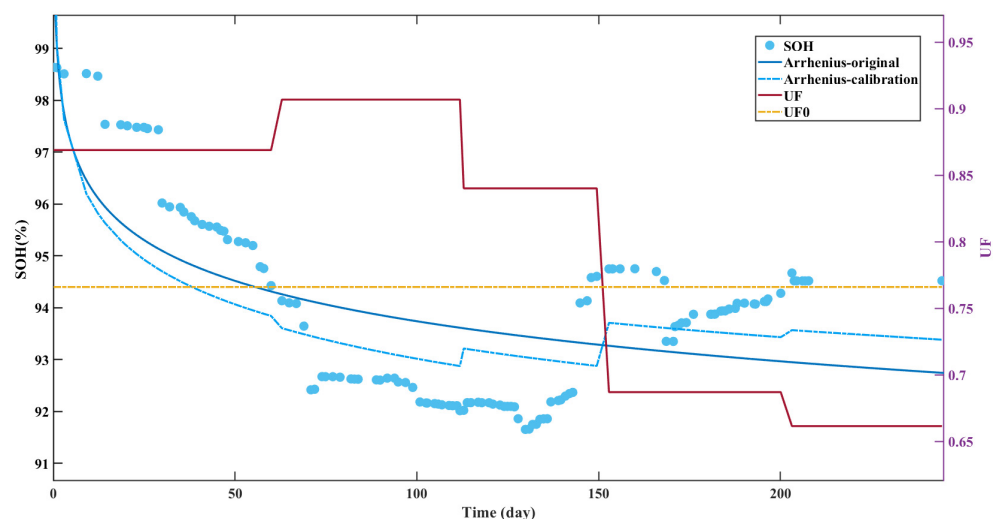


Figure 8. An example of the calibration effects of the UF for battery lifetime degradation. The results come from the calculation of the UF calibration with a certain PHEV. A UF₀ needed to be pre-determined to apply Equations (9) and (10), which is discussed in the following section.

3. Experiment Results and Evaluation

3.1. Experiment Results

We obtained the discrete SOH value SOH_o for every vehicle introduced in Section 2.1 (there are 11 vehicles, with the numbers ranging from 1 to 11) using the accumulated SOC-capacity method shown in Equation (2) and (3), and then we fitted the SOH prediction curve using the Arrhenius equation. As described in Section 2.3.2, PHEVs operate under dynamic conditions rather than pure electric drive; as such, the parameter z in the Arrhenius equation can be adjusted by different UF conditions with the fuzzy logic algorithm to further refine the SOH.

3.1.1. Optimal UF Selection

Because the SOH is a low-frequency parameter that can be estimated (excluding sudden drops of capacity), it does not rapidly change within every cycle. Hence, even though every charge and discharge cycle has a UF value, we only apply the average of all discrete UF values in a fixed cycle range. Therefore, for the value of the UF, we calculate the average of all discrete UF values within a fixed cycle interval N_0 as the final UF value to be used for calibration, as shown in the equation below:

$$\text{UF}_C = \frac{\sum \text{UF}}{N_0} \quad (11)$$

where UF_C represents the average UF value within a fixed cycle range and N_0 represents a fixed number of cycles, which can be divided into 10, 20, 30, 40, and 50. The sum of UF within every fixed cycle number is denoted by $\sum \text{UF}$, and one cycle means a charge or discharge cycle.

For the optimization of the effects of threshold UF_0 and UF_C on the calibration results, we designed a verification scheme as follows.

- (1) Step 1: the average UF values UF_C are calculated according to Equation (11) using different fixed cycle intervals (10, 20, 30, 40, and 50).
- (2) Step 2: the vehicle dataset is divided into two datasets as the calibration dataset and testing dataset. Based on the two datasets, the optimal threshold UF_0 was determined using a certain optimal index that was calculated on the two datasets and the whole vehicle dataset.
- (3) Step 3: the calibration effects on the two datasets and the whole vehicle dataset were discussed. Then, the calibration effects of the optimal threshold UF_0 in different fixed cycle intervals were also compared.
- (4) Step 4: the average UF values UF_C in different fixed cycle intervals were discussed to choose the optimal fixed cycle interval for practical calibration.

In Step 1, the average UF values are calculated and presented in Figure 9 according to Equation (11) using different fixed cycle intervals (10, 20, 30, 40, and 50). From Figure 9a, the original UF point distribution is relatively messy and has no obvious distribution pattern. The change in the trend of UF mean values in the different cycle intervals is generally the same, but the difference lies in the change in amplitude of UF mean values in different cycle intervals.

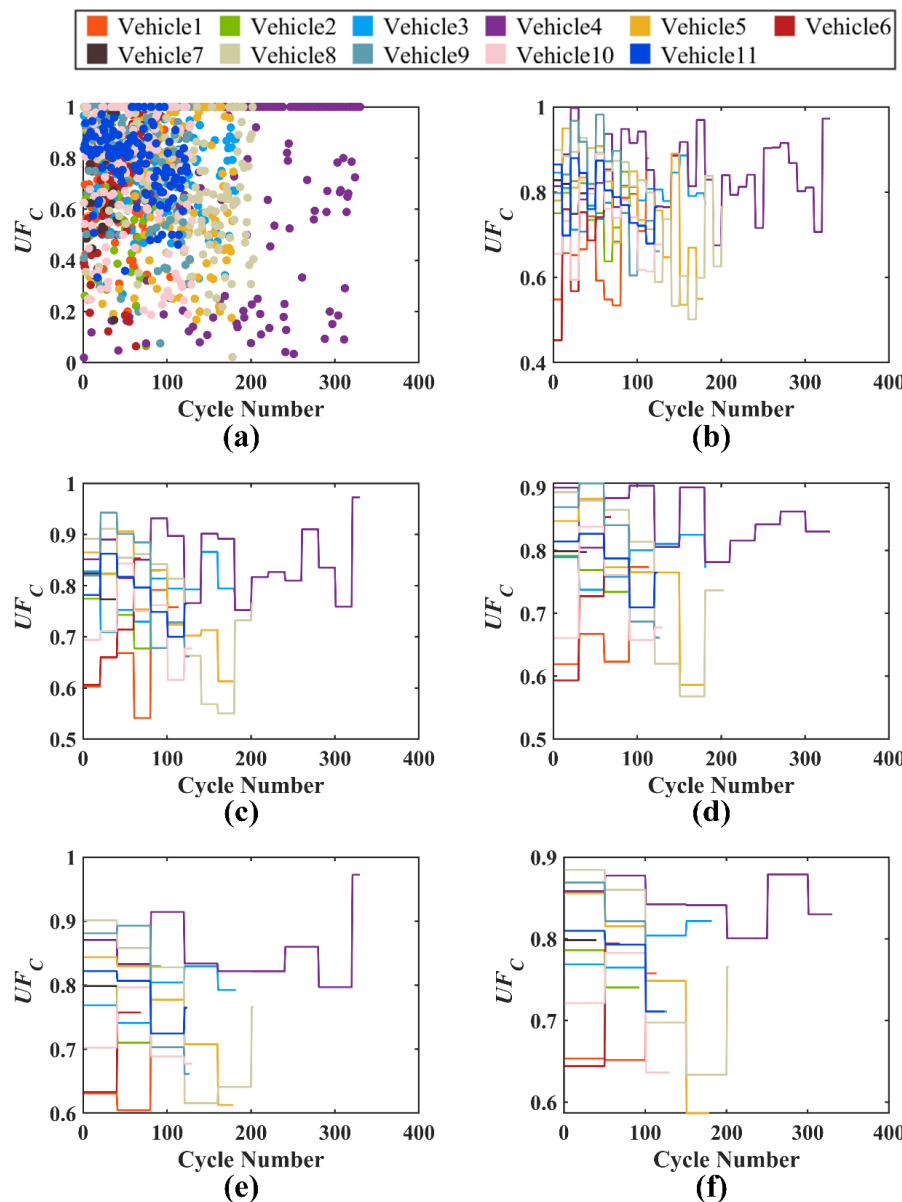


Figure 9. The UF_C of different cycles N_0 . (a) $N_0 = 1$. (b) $N_0 = 10$. (c) $N_0 = 20$. (d) $N_0 = 30$. (e) $N_0 = 40$. (f) $N_0 = 50$.

In Step 2, the UF_0 value range was set to $[0.06, 0.09]$ with an interval of 0.001, which was based on the UF variation range of all vehicles. On the above settings, we used all 11 vehicles as the entire set to search for the optimal threshold UF_0 ; we also randomly divided the 11 vehicles into a calibration set and a validation set. Six vehicles were selected as the calibration set, which were numbered 1–6, and five vehicles were selected as the test set, numbered 7–11. The two methods of using the entire set and distinguishing between the calibration and validation sets were employed to validate the effectiveness of this calibration approach. With the pre-determined UF fixed cycle numbers N_0 (10, 20, 30, 40, 50), the optimal threshold UF_0 for the entire set was searched; then, the optimal threshold UF_0 for the calibration set and validation set was also searched, respectively. The root mean square error (RMSE) was used as the criterion for determining the optimal threshold UF_0 . The RMSE was calculated from the discrete points of calibrated SOH values and the original SOH, as shown in Equation (12).

$$RMSE = \sqrt{\sum_{i=1}^n \frac{(SOH_{ci} - SOH_{oi})}{n}} \quad (12)$$

where SOH_{ci} is the i -th calibrated SOH value, SOH_{oi} is the i -th original SOH discrete value, and n is the vehicle operation cycles. The calculated optimal UF_0 values are shown in Table 4.

Table 4. The optimal results of UF_0 .

Sets \ N_0	10	20	30	40	50
Entire set	0.765	0.764	0.764	0.764	0.764
Calibration set	0.776	0.775	0.775	0.776	0.774
Test set	0.760	0.759	0.759	0.759	0.760

In Table 4, it can be seen that the results for $N_0 = 20$ and $N_0 = 30$ are the same, while the values for $N_0 = 10$, $N_0 = 40$, and $N_0 = 50$ in the same dataset are close to equal. However, this method only seeks an optimization through a comparison of different UF_0 values, and the actual calibration effect needs to be verified by comparing it with the uncalibrated results, i.e., by verifying the calibration effect of the selected optimal UF_0 on the validation set. The verification parameters are the RMSE and the coefficient of determination (R^2); RMSE represents the absolute error of the fit, and R^2 represents the goodness of fit. The specific approach used was to compare the RMSE between the fitted values before and after calibration and the original discrete SOH values, as well as with the R^2 values before and after calibration. Smaller RMSE and a larger R^2 values are preferred.

$$R^2 = 1 - \frac{\sum_{i=1}^n (\text{SOH}_{oi} - \text{SOH}_{ci})^2}{\sum_{i=1}^n (\text{SOH}_{oi} - \bar{\text{SOH}}_o)^2} \quad (13)$$

where SOH_{ci} represents the i -th calibrated SOH value, SOH_{oi} represents the i -th original discrete SOH values, n is the vehicle operation cycles, and $\bar{\text{SOH}}_o$ is the mean value of the original discrete SOH values.

In Step 3, after the determination of optimal threshold UF_0 , the effects when using two different datasets and the whole dataset were discussed; the optimal threshold UF_0 in different fixed cycle intervals were also discussed. The RMSE results for all fixed cycles are presented in Figure 10, where the orange bars are the results for the calibration and validation sets. Vehicle1–6 were calibrated using the optimal threshold UF_0 of the calibration set, while vehicle7–11 were calibrated using the optimal threshold UF_0 of the validation set. The green bars represent the results for the entire set, with vehicle1–11 being calibrated using the optimal threshold UF_0 of the entire set. The blue bars are the uncalibrated vehicles. Figure 11 shows the R^2 results for all fixed cycles: the orange lines indicate the results from the calibration and validation sets, where vehicle1–6 used the optimal threshold UF_0 from the calibration set and vehicle7–11 used the optimal threshold UF_0 from the validation set. The green line represents the overall results, with all vehicles (1–11) using the optimal threshold UF_0 from the entire dataset for calibration. The blue line illustrates the results without any calibration. It can be seen from the figure that, for the vehicles having a smaller RMSE after calibration compared with before, their R^2 after calibration was larger than before.

In Step 4, after the analysis of the calibration effects of optimal threshold UF_0 values, the next step involves determining the fixed cycle interval for practical calibration. The statistical analysis of the calibration effect of different cycle intervals is shown in Table 5. From Table 5, it can be noted that when $N_0 = 30$, there are five vehicles with a positive calibration effect, which is the highest number of fixed cycles with a positive calibration effect among all N_0 values. Therefore, $N_0 = 30$ was chosen as the optimal fixed cycle number.

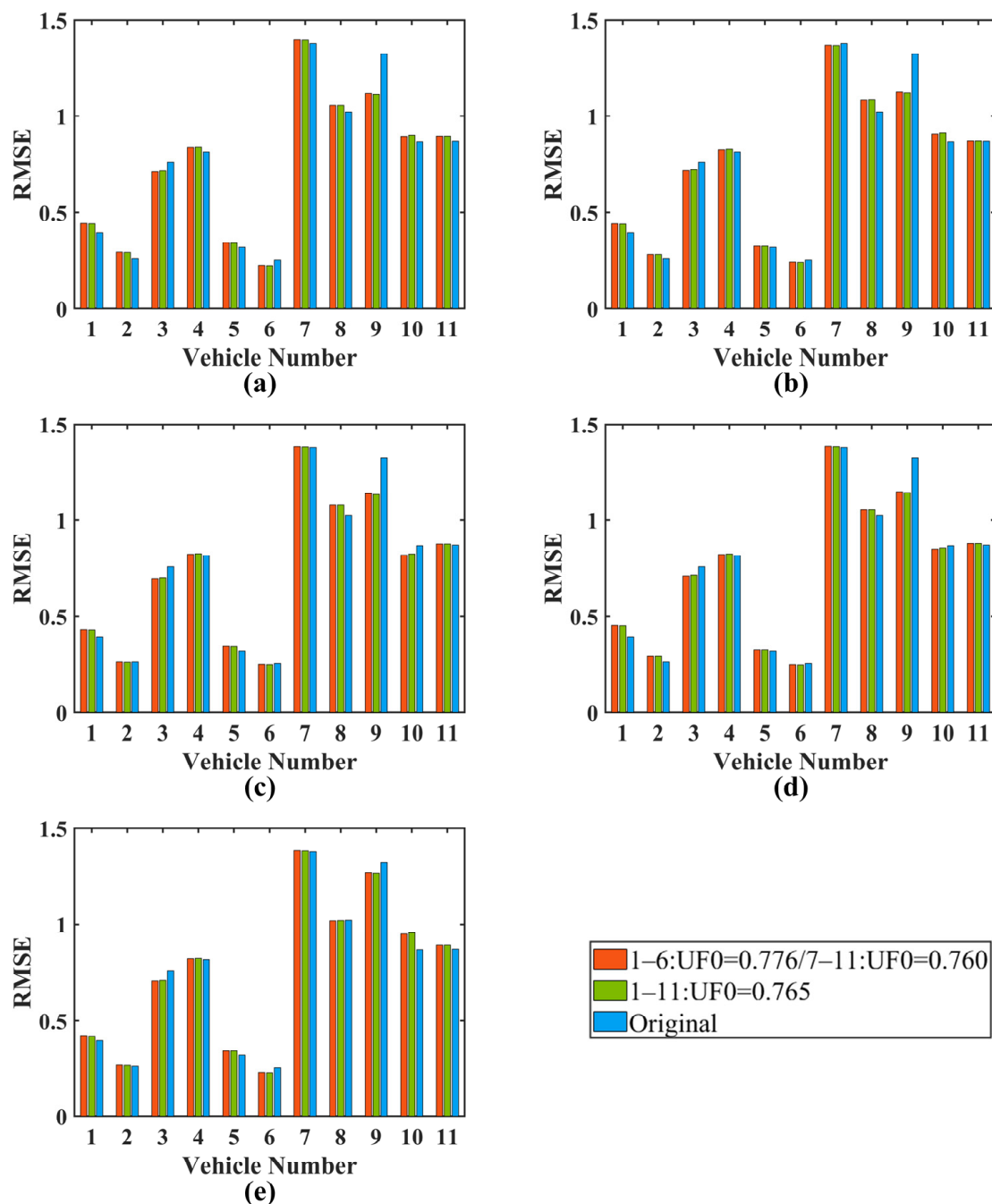


Figure 10. The RMSEs of different cycles N_0 . **(a)** $N_0 = 10$. **(b)** $N_0 = 20$. **(c)** $N_0 = 30$. **(d)** $N_0 = 40$. **(e)** $N_0 = 50$.

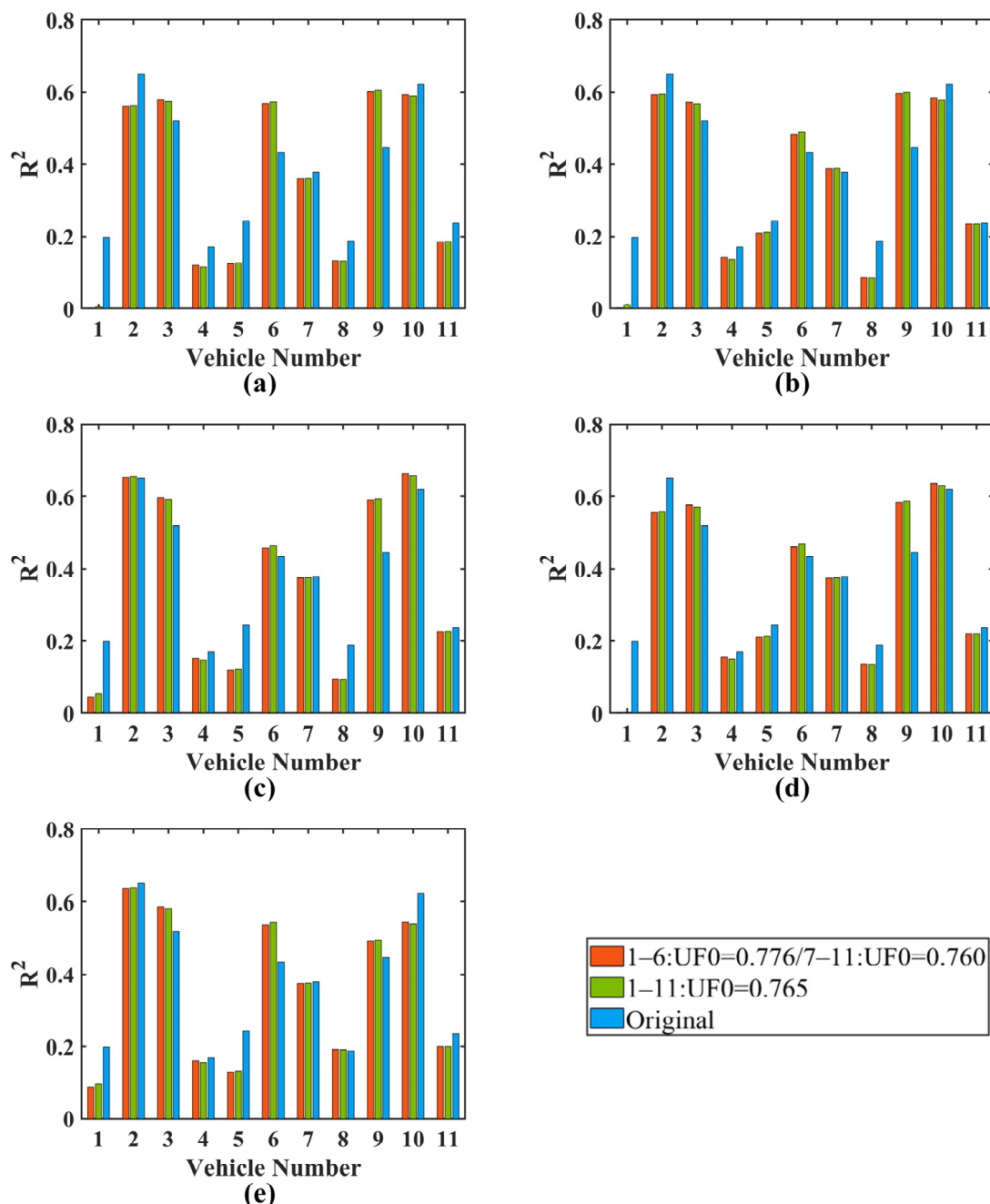


Figure 11. The R^2 values of different cycles N_0 . (a) $N_0 = 10$. (b) $N_0 = 20$. (c) $N_0 = 30$. (d) $N_0 = 40$. (e) $N_0 = 50$.

Table 5. Calibration effects at different cycle intervals.

Effects	N_0				
	10	20	30	40	50
Vehicle with positive calibration	3, 6, 9	3, 6, 7, 9	2, 3, 6, 9, 10	3, 6, 9, 10	3, 6, 8, 9
Vehicle with negative calibration	1, 2, 4, 5, 7, 8, 10, 11	1, 2, 4, 5, 8, 10, 11	1, 4, 5, 7, 8, 11	1, 2, 4, 5, 7, 8, 11	1, 2, 4, 5, 7, 10, 11
Amount of positive calibration	3	4	5	4	4

3.1.2. Calibration Results on Vehicle SOH Prediction

After reviewing Figures 10 and 11 it can be observed that when searching for the optimal threshold UF_0 for calibration through the entire set, there were five vehicles with

positive calibration effects at $N_0 = 30$. When searching for the optimal threshold UF_0 by distinguishing between the calibration set and the validation set, the vehicles with positive calibration effects at $N_0 = 30$ were the same as those obtained by using the entire set, which verifies the effectiveness of using the UF to calibrate the SOH of PHEVs. Therefore, the optimal threshold UF_0 obtained from the calibration set was used as the final UF_0 for calibrating the SOH of the validation set.

Figure 12 depicts the SOH curves of vehicles exhibiting a positive calibration effect; Figure 13 shows the SOH curves of vehicles displaying a negative calibration effect. From Figure 12, it is evident that the discrete SOH values fluctuate due to variations in the operating conditions of the vehicles. Despite the fluctuations in the discrete SOH values, the initial Arrhenius curve gradually decreases, which aligns with the expected characteristics of SOH change. Through the process of discretization and calibration of the original Arrhenius fitting curve, the discrete Arrhenius curves for different cycles will either converge closer or diverge farther away from the discrete SOH values.

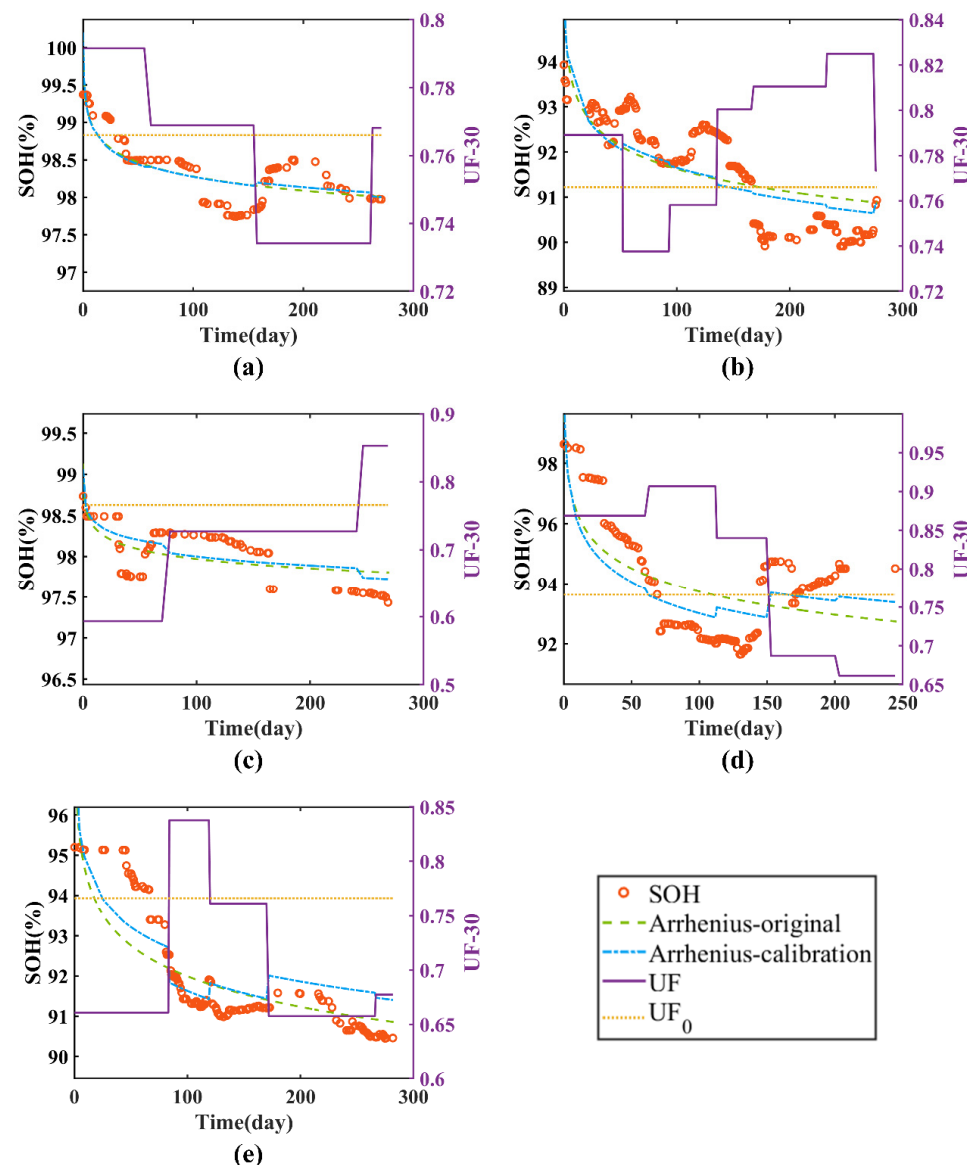


Figure 12. Positive calibration effect vehicle curve. (a) Vehicle2. (b) Vehicle3. (c) Vehicle6. (d) Vehicle9. (e) Vehicle10. The red circles are the discrete values of the SOH under different cycles, the black dashed line is the original Arrhenius fitting curve, the green dotted line is the Arrhenius fitting curve after calibration, the purple solid line is the UF value, and the pink dotted line is the UF_0 .

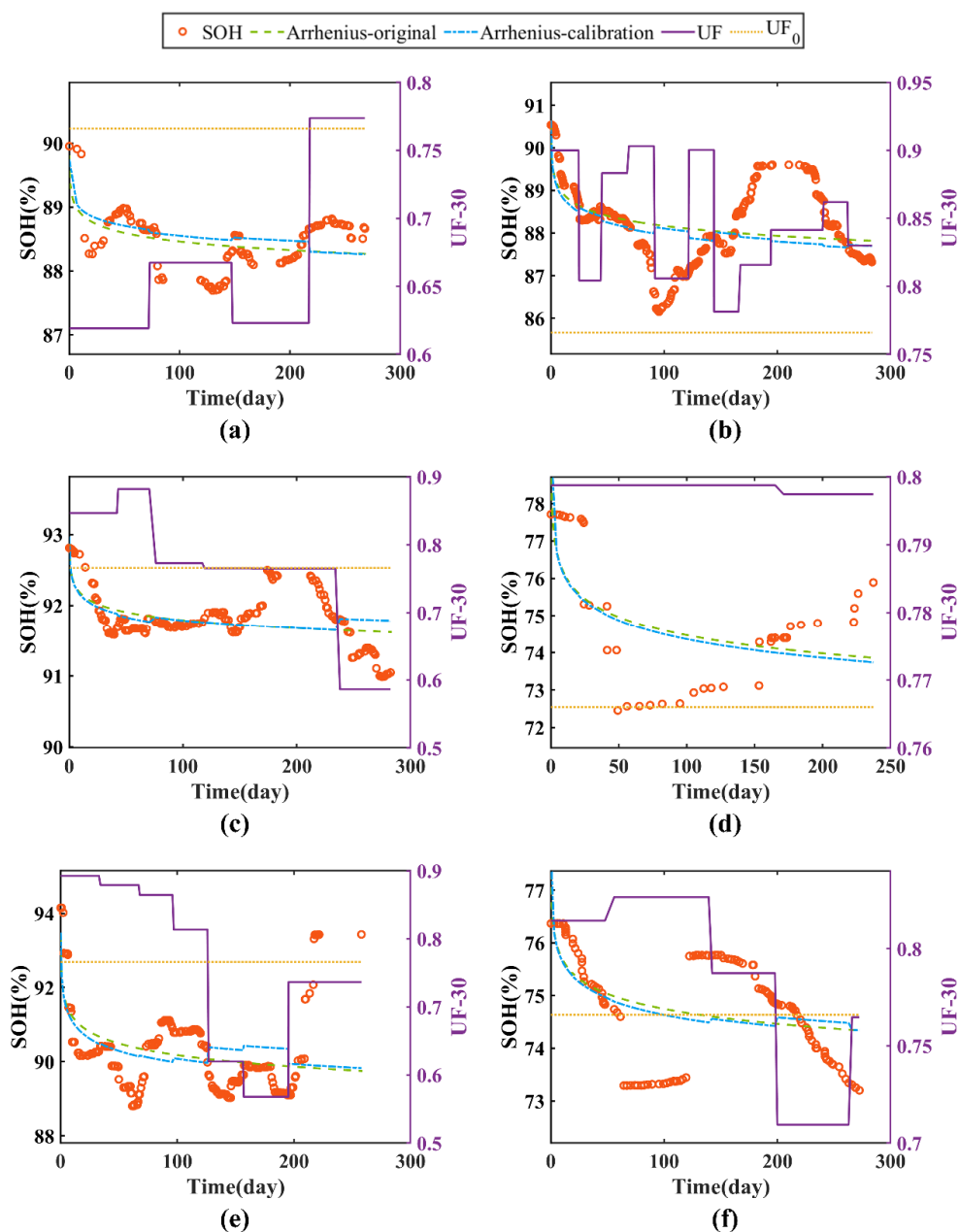


Figure 13. Negative calibration effect vehicle curve. (a) Vehicle1. (b) Vehicle4. (c) Vehicle5. (d) Vehicle7. (e) Vehicle8. (f) Vehicle11. The red circles are the discrete values of SOH under different cycles, the black dashed line is the original Arrhenius fitting curve, the green dotted line is the Arrhenius fitting curve after calibration, the purple solid line is the UF value, and the pink dotted line is the UF_0 .

By comparing Figures 12 and 13, it becomes evident that if a greater number of discrete Arrhenius curves align closely with the SOH discrete values, it indicates a positive calibration effect. Conversely, if a larger proportion of discrete Arrhenius curves deviates further from the SOH discrete values, it indicates a negative calibration effect. From the analysis of the curve change, it can be inferred that the relationship between UF and UF_0 is the factor that affects the deviation direction of the discrete Arrhenius curve. If UF is smaller than UF_0 , the calibrated parameter z is smaller than the original value, and the final discrete Arrhenius value will be larger than the original value. If UF is larger than UF_0 , the calibrated parameter z is larger than the original value, and the final discrete Arrhenius value will be smaller than the original value.

3.2. Calibration Effectiveness

From Figures 12 and 13, it is evident that UF calibration can have both positive and negative effects on the fitting degradation curve of PHEV batteries. However, aside from the UF, other factors may also influence the effectiveness of UF calibration. In this section, we aim to explore the underlying reasons and suitable conditions for UF calibration. To this end, we conducted a correlation analysis, shown in Figure 5, and calculated the mean values (presented in Table 6) and variances (presented in Table 7) of nine factors/dimensions that are related to the SOH. We compared these mean and variance values to identify any significant differences. For illustrative purposes, we divided the 11 vehicles in the dataset into two groups: vehicles with positive UF (vehicle2, vehicle3, vehicle6, vehicle9, vehicle10) and vehicles with negative UF (vehicle1, vehicle4, vehicle5, vehicle7, vehicle8, vehicle11). The comparison of the mean and variance values between these two groups is presented in Figures 14 and 15.

Table 6. Mean of nine factors related to the SOH for the vehicle dataset (including the SOH).

Vehicle Number	Start Charging SOC	Charging Duration	PTA60	Charging Rate	Discharging Rate	DVKT	E-CVKT	DOC	SOH	UF
Vehicle1	18.3333	3.0907	0.1830	-90.2240	0.4113	27.6833	51.6140	77.7544	88.4334	0.6654
Vehicle2 *	31.2151	1.3422	0.2745	-0.2714	0.7077	34.4961	66.9247	37.9677	98.3576	0.7650
Vehicle3 *	18.8022	2.4672	0.3492	-0.2641	0.5434	36.8714	56.4286	70.3132	91.6116	0.7867
Vehicle4	41.0091	2.9802	0.3585	-0.0864	0.6386	41.8517	39.7039	50.6707	88.1795	0.8484
Vehicle5	19.8045	2.4352	0.4264	-0.2628	0.6197	31.3655	46.7263	68.9050	91.8248	0.7708
Vehicle6 *	36.4857	1.6542	0.1682	-0.2689	0.4479	67.7194	114.5714	45.3143	98.0118	0.6869
Vehicle7	21.3000	5.6298	0.0865	-0.0880	0.4593	55.1220	61.9500	60.0500	74.8514	0.7984
Vehicle8	27.3054	2.4416	0.1552	-0.2517	0.4370	42.4369	38.4483	64.2365	90.3339	0.7688
Vehicle9 *	21.3386	2.6462	0.2336	-0.2641	0.4946	47.3295	57.7402	71.7087	93.7153	0.8166
Vehicle10 *	19.8154	2.5214	0.1560	-0.2683	0.4252	61.9287	50.3846	74.2308	91.9104	0.7253
Vehicle11	11.0403	5.4652	0.0707	-0.1027	0.4461	21.6249	39.2500	61.6774	74.6177	0.7838

* Rows in blue color are the vehicles with positive calibration, that is, Vehicle2, Vehicle3, Vehicle6, Vehicle9, and Vehicle10.

Table 7. Variance of nine factors related to the SOH for the vehicle dataset (including the SOH).

Vehicle Number	Start Charging SOC	Charging Duration	PTA60	Charging Rate	Discharging Rate	DVKT	E-CVKT	DOC	SOH	UF
Vehicle1	313.9764	0.5984	0.0048	0.0001	0.0131	334.8532	7975.6550	401.8683	0.0308	0.0371
Vehicle2 *	636.7576	1.0926	0.0156	0.0000	0.0610	315.9398	4548.3747	906.4881	0.1291	0.0575
Vehicle3 *	425.1098	0.8166	0.0100	0.0001	0.0182	652.7748	4736.5114	709.0561	0.6200	0.0310
Vehicle4	392.5302	2.6077	0.0310	0.0000	0.0544	1871.7027	826.2454	620.2640	0.1366	0.0810
Vehicle5	270.3941	0.7513	0.0174	0.0001	0.0248	365.9159	617.7168	630.7943	0.0401	0.0670
Vehicle6 *	966.6302	1.2820	0.0173	0.0002	0.0112	9389.7177	18,610.7702	994.2766	0.0408	0.0496
Vehicle7	363.4462	7.5441	0.0194	0.0002	0.0164	6124.3277	4429.4846	945.7410	1.1835	0.0532
Vehicle8	611.4607	1.6979	0.0271	0.0024	0.0237	4011.1059	1080.0010	767.7854	0.2517	0.0510
Vehicle9 *	307.5273	1.2750	0.0143	0.0011	0.0279	3289.4916	16,368.9240	451.8906	0.6160	0.0522
Vehicle10 *	242.1827	0.4657	0.0303	0.0005	0.0096	3302.4934	988.7346	496.4890	1.3840	0.0629
Vehicle11	152.7219	7.7078	0.0021	0.0016	0.0075	539.0179	306.5630	907.7488	0.2238	0.0185

* Rows in blue color are the vehicles with positive calibration, that is, Vehicle2, Vehicle3, Vehicle6, Vehicle9, and Vehicle10.

In Figure 14, vehicles with a positive UF are in the blue series, while vehicles with a negative UF are in the orange series. Due to various value ranges, the nine factors are divided into two subfigures as Figure 14a,b. Except for the UF, DVKT, E-CVKT, and SOH in Figure 14a, the charging duration and charging rate in Figure 14b exhibit obvious difference. Vehicles with positive UF effects hold a smaller charging duration, while vehicles with negative UF effects hold smaller DVKT, E-CVKT, charging rate, and SOH values. The SOH of the vehicles with negative UF effects were even lower than 80%, which were considered as retired vehicles. The difference of all factors shows that the vehicles with negative UF effects are vehicles with heavier degradation. Hence, when the vehicle gradually falls into

an unhealthy state, the Arrhenius method cannot fit the battery degradation well; thus, the UF calibration may also not bring positive calibration effects. In conclusion, the proposed UF calibration method may not be suitable for vehicles with heavy degradation, and future work should focus on the heavy degradation conditions.

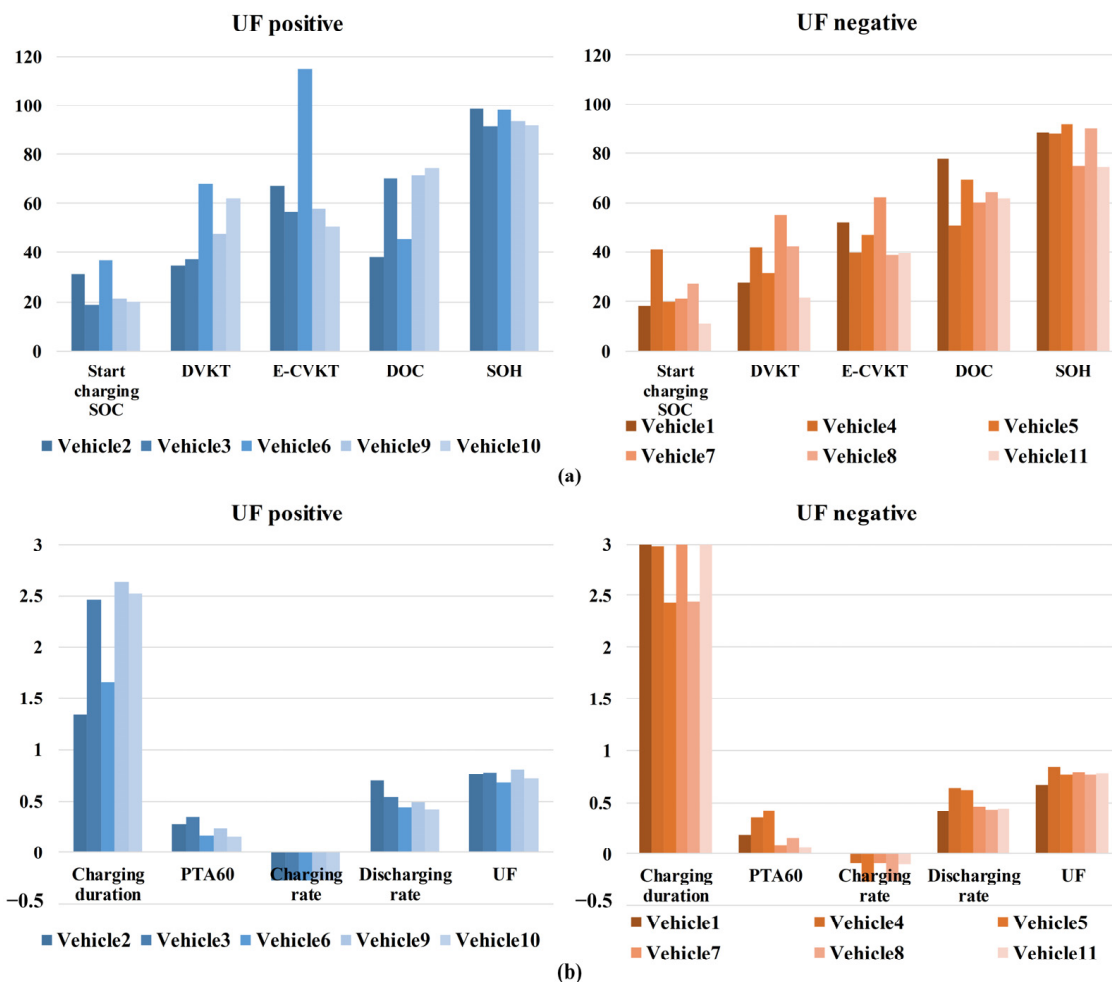


Figure 14. Comparison of the mean of the nine selected factors/dimensions when the UF was positive (blue series) and the UF was negative (orange series). In the figure, the x-axis consists of the nine dimensions as shown in Table 6; the y-axis is the mean value of every dimension. The nine factors are divided into two subfigures due to the y-axis range: (a) start charging SOC, DVKT, E-CVKT, DOC, and SOH; (b) charging duration, PTA60, charging rate, discharging rate, and UF. In every subfigure, the 11 vehicles in the vehicle dataset are compared as vehicles with a positive UF (vehicle2, vehicle3, vehicle6, vehicle9, and vehicle10), and vehicles with a negative UF (vehicle1, vehicle4, vehicle5, vehicle7, vehicle8, and vehicle11).

As for the variance comparison shown in Figure 15, it can be obtained that the start charging SOC, DVKT, E-CVKT, and DOC hold large variance values, while the PTA60, charging rate, discharging rate, and UF hold small values. Only the E-CVKT variance of Vehicles with positive UF effects were larger than that of vehicles with negative UF effects. The other eight factors did not show obvious rules between positive UF and negative UF effects. Because variance means the discrete extent of the dataset, the larger E-CVKT variance does not bring significant change to the UF calibration effects. Hence, in the variance aspect, we did not find any determined influence of the nine factors on the calibration effects.

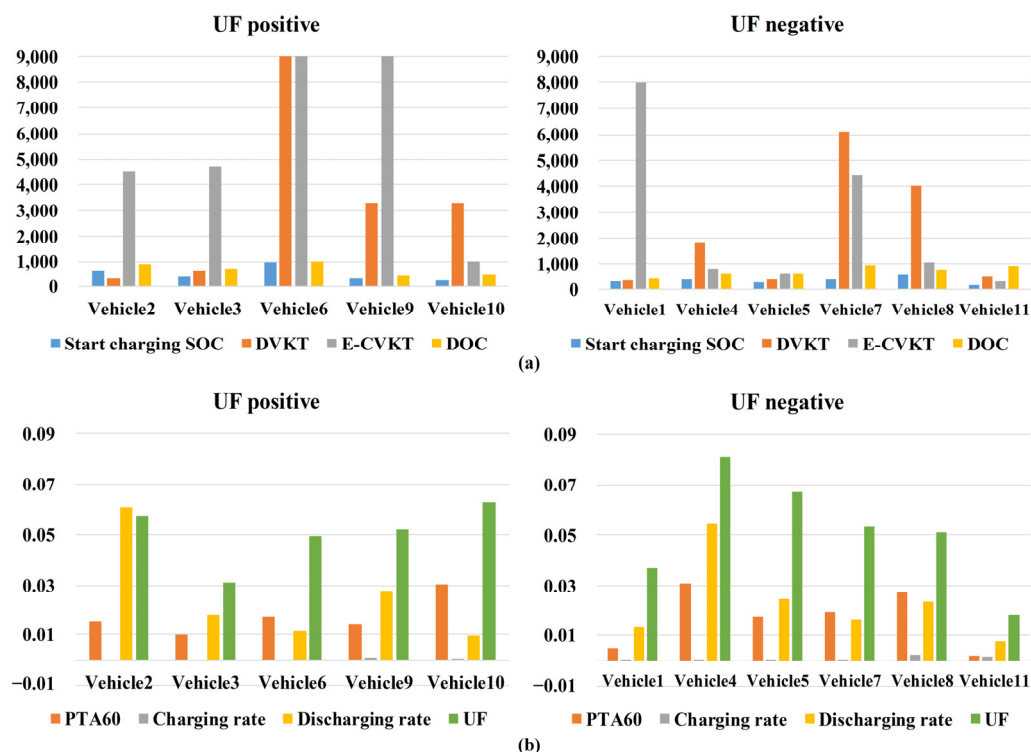


Figure 15. Comparison of the variance of the nine selected factors/dimensions when the UF was positive (left) and the UF was negative (right). In the figure, the x-axis is the vehicle number, and y-axis is the variance value of every dimension. Only eight factors were divided into two subfigures due to the y-axis range: (a) start charging SOC, DVKT, E-CVKT, and DOC; (b) PTA60, charging rate, discharging rate, and UF. The charging duration is not shown in the figure due to its irregularity.

3.3. Discussion

Several key points for the results part are presented as follows:

- (1) For the 11 PHEVs in this work, the best UF calibration value was 0.776 and the best calibration cycle interval was 30. Using the best UF value and best cycle interval, the proposed calibration scheme can achieve an optimized calibration effects of SOH prediction for any set of PHEVs with a realistic dataset.
- (2) The results show that a discrete Arrhenius curve is achieved after UF calibration, and the Arrhenius curve is no longer monotonous like a traditional battery degradation curve. We believe that the battery SOH should be discrete and fluctuant in every certain range after considering UF's influence.
- (3) According to Section 3.1.1, the UF threshold was optimized by using a pre-designed scheme that included the training vehicle dataset. It was found that the value of the UF threshold can be in a range to generate homogeneous calibration effects (positive or negative).
- (4) The proposed UF calibration method did have positive effects (smaller RMSE and larger R^2) on some of the PHEVs. However, it showed negative effects for PHEVs with heavy degradation due to the inapplicability of Arrhenius fitting when the PHEV has large capacity loss.

4. Conclusions

In order to better predict the battery degradation of PHEVs, this work included actual PHEV driving patterns into the SOH calculation by calibrating using the SOH Arrhenius method. Using the realistic operation data of a set of 11 PHEVs in Chongqing with 13,590 km and 233 average driving days, most of the vehicles' travel mileage was determined to be driven by electricity, which stresses the importance of PHEV battery

degradation research. By comparing the correlation coefficients between each driving feature parameter and the SOH, the UF was selected to calibrate the SOH of the PEHVs due to the highest coefficient. The calibration method introduced a fuzzy UF relationship to the Arrhenius equation. By setting up test sets, validation sets, and whole sets, the discrete Arrhenius trend of battery SOH was formed using UF average values under different cycle intervals. By comparing the RMSE and R^2 of the calibrated SOH with those of the uncalibrated SOH, the calibration results under different cycle intervals were statistically analyzed to determine the best UF calibration value and the best correction cycle interval. The experiment results showed that the root mean square error (RMSE) of the SOH fitting after UF calibration could be decreased by 0.2–14%, and the coefficient of determination (R^2) for calibrated fitting trends could be improved by 0.5–32%. The results also showed that some vehicles (five vehicles) could be positively calibrated, while the others (six vehicles) could only be negatively calibrated. In response to this result, we conducted a comparative analysis from multiple dimensions and found that the proposed UF calibration method may not always be suitable for PHEVs with heavy degradation.

Based on the summary of the work content above, we can see that the SOH estimation calibration method proposed in this paper for the complex operating conditions of PHEVs has a good calibration effect, which can make the estimated SOH closer to the true value, and this provides a guarantee for more reasonable battery safety management. However, this method still has some room for improvement so that it can be applied to operating conditions with severe battery aging. Therefore, our future research will consider how to reasonably calibrate the PHEV's SOH through the actual vehicle operation characteristics of PHEVs in a wider life cycle. Compared with EVs, more factors that are unique to PHEVs for SOH calibration still need further experiment and data analysis, and they are worth exploring in the future.

Moreover, it is important to acknowledge that this research is constrained by limitations in data availability, the sample size, and the absence of battery temperature data. These factors may contribute to some fluctuations in the values obtained. However, despite these limitations, the methodology employed in this study provides valuable insights for estimating the SOH of PHEVs. In future research endeavors, it is recommended to incorporate a larger and more diverse dataset that includes battery temperature information; this will allow for a more comprehensive validation of the methodology's effectiveness by analyzing a broader range of PHEVs. By addressing these limitations and expanding the scope of data collection, we can further enhance the accuracy and reliability of SOH estimation methodologies for PHEVs. This would contribute to the advancement of knowledge in the field and provide more robust guidance for PHEV battery management and maintenance practices.

Author Contributions: Conceptualization, H.C. and X.H. (Xu Hao); methodology, H.C., X.H. (Xu Hao), Y.J. and Y.W.; software, H.C. and Y.J.; validation, H.C. and Y.J.; formal analysis, H.C., X.H. (Xu Hao), Y.J. and Y.W.; investigation, H.C., Y.J. and Y.Y.; resources, X.H. (Xu Hao) and Y.J.; data curation, Y.Y., X.H. (Xu Hao) and H.W.; writing—original draft preparation, H.C., X.H. (Xu Hao), Y.J. and Y.W.; writing—review and editing, X.H. (Xuebing Han), H.W. and Y.Z.; supervision, Y.Z., H.W. and M.O.; project administration, X.H. (Xuebing Han) and H.W.; funding acquisition, H.W., Y.W. and M.O. All authors have read and agreed to the published version of the manuscript.

Funding: This research was funded by the Chongqing Science and Technology Commission [Chongqing Technology Innovation and Application Development Special Key Project cstc2019jscx-zdztzx0048], National Natural Science Foundation of China under Grant No. 62103220, and High-safety, All-Climate Power Battery and Electric Chassis Integrated Design and Development program [TC210H02R].

Data Availability Statement: Not applicable.

Conflicts of Interest: The authors declare no conflict of interest.

Abbreviations

BEV	Battery electric vehicle
DOC	Depth of charge
CVKT	Vehicle kilometers travelled during two charging sessions
DAAM	Discrete Arrhenius aging model
DVKT	Daily vehicle kilometers travelled
E-CVKT	Vehicle kilometers travelled during two charging sessions driven by electricity
CD	charging depleting
PEV	Plug-in electric vehicle
PHEV	Plug-in hybrid electric vehicle
PTA60	Percentage of miles traveled above 60 km/h
RMSE	Root mean square error
SOC	State of charge
SOH	State of health
UF	Utility factor

References

1. International Energy Agency. *Global EV Outlook 2022*; IEA: Paris, France, 2022.
2. Lopez-Ibarra, J.A.; Goitia-Zabaleta, N.; Isaac Herrera, V.; Gazta Naga, H.; Camblong, H. Battery aging conscious intelligent energy management strategy and sensitivity analysis of the critical factors for plug-in hybrid electric buses. *eTransportation* **2020**, *5*, 100061. [[CrossRef](#)]
3. Ouyang, D.; Zhang, Q.; Ou, X. Review of Market Surveys on Consumer Behavior of Purchasing and Using Electric Vehicle in China. In Proceedings of the Applied Energy Symposium and Forum—Low-Carbon Cities and Urban Energy Systems (CUE), Shanghai, China, 5–7 June 2018; pp. 612–617.
4. Hao, X.; Yuan, Y.; Wang, H.; Ouyang, M. Plug-in hybrid electric vehicle utility factor in China cities: Influencing factors, empirical research, and energy and environmental application. *eTransportation* **2021**, *10*, 100138. [[CrossRef](#)]
5. Zubi, G.; Dufo-López, R.; Carvalho, M.; Pasaoglu, G. The lithium-ion battery: State of the art and future perspectives. *Renew. Sustain. Energy Rev.* **2018**, *89*, 292–308. [[CrossRef](#)]
6. Wassiliadis, N.; Steinstraeter, M.; Schreiber, M.; Rosner, P.; Nicoletti, L.; Schmid, F.; Ank, M.; Teichert, O.; Wildfeuer, L.; Schneider, J.; et al. Quantifying the state of the art of electric powertrains in battery electric vehicles: Range, efficiency, and lifetime from component to system level of the Volkswagen ID.3. *eTransportation* **2022**, *12*, 100167. [[CrossRef](#)]
7. Liu, K.; Liu, Y.Y.; Lin, D.C.; Pei, A.; Cui, Y. Materials for lithium-ion battery safety. *Sci. Adv.* **2018**, *4*, eaas9820. [[CrossRef](#)] [[PubMed](#)]
8. Fotouhi, A.; Auger, D.J.; Propp, K.; Longo, S.; Wild, M. A review on electric vehicle battery modelling: From Lithium-ion toward Lithium-Sulphur. *Renew. Sustain. Energy Rev.* **2016**, *56*, 1008–1021. [[CrossRef](#)]
9. Tian, H.X.; Qin, P.L.; Li, K.; Zhao, Z. A review of the state of health for lithium -ion batteries: Research status and suggestions. *J. Clean. Prod.* **2020**, *261*, 120813. [[CrossRef](#)]
10. Berecibar, M.; Gandiaga, I.; Villarreal, I.; Omar, N.; Van Mierlo, J.; Van den Bossche, P. Critical review of state of health estimation methods of Li-ion batteries for real applications. *Renew. Sustain. Energy Rev.* **2016**, *56*, 572–587. [[CrossRef](#)]
11. Zhang, J.; Lee, J. A review on prognostics and health monitoring of Li-ion battery. *J. Power Sources* **2011**, *196*, 6007–6014. [[CrossRef](#)]
12. Zhang, H.; Qin, Y.; Li, X.; Liu, X.; Yan, J. Power management optimization in plug-in hybrid electric vehicles subject to uncertain driving cycles. *eTransportation* **2020**, *3*, 100029. [[CrossRef](#)]
13. Li, X.; Yuan, C.; Wang, Z.; He, J.; Yu, S. Lithium battery state-of-health estimation and remaining useful lifetime prediction based on non-parametric aging model and particle filter algorithm. *eTransportation* **2022**, *11*, 100156. [[CrossRef](#)]
14. Song, Z.; Yang, X.-G.; Yang, N.; Delgado, F.P.; Hofmann, H.; Sun, J. A study of cell-to-cell variation of capacity in parallel-connected lithium-ion battery cells. *eTransportation* **2021**, *7*, 100091. [[CrossRef](#)]
15. Berecibar, M.; Garmendia, M.; Gandiaga, I.; Crego, J.; Villarreal, I. State of health estimation algorithm of LiFePO₄ battery packs based on differential voltage curves for battery management system application. *Energy* **2016**, *103*, 784–796. [[CrossRef](#)]
16. Goh, T.; Park, M.; Seo, M.; Kim, J.G.; Kim, S.W. Capacity estimation algorithm with a second-order differential voltage curve for Li-ion batteries with NMC cathodes. *Energy* **2017**, *135*, 257–268. [[CrossRef](#)]
17. Li, X.; Wang, Z.; Zhang, L.; Zou, C.; Dorrell, D.D. State-of-health estimation for Li-ion batteries by combining the incremental capacity analysis method with grey relational analysis. *J. Power Sources* **2019**, *410*, 106–114. [[CrossRef](#)]
18. Zheng, L.; Zhu, J.; Lu, D.D.-C.; Wang, G.; He, T. Incremental capacity analysis and differential voltage analysis based state of charge and capacity estimation for lithium-ion batteries. *Energy* **2018**, *150*, 759–769. [[CrossRef](#)]
19. Jiang, B.; Dai, H.; Wei, X. Incremental capacity analysis based adaptive capacity estimation for lithium-ion battery considering charging condition. *Appl. Energy* **2020**, *269*, 115074. [[CrossRef](#)]

20. Zhu, J.G.; Wang, Y.X.; Huang, Y.; Gopaluni, R.B.; Cao, Y.K.; Heere, M.; Muhlbauer, M.J.; Mereacre, L.; Dai, H.F.; Liu, X.H.; et al. Data-driven capacity estimation of commercial lithium-ion batteries from voltage relaxation. *Nat. Commun.* **2022**, *13*, 2261. [[CrossRef](#)]
21. Qian, C.; Xu, B.; Chang, L.; Sun, B.; Feng, Q.; Yang, D.; Ren, Y.; Wang, Z. Convolutional neural network based capacity estimation using random segments of the charging curves for lithium-ion batteries. *Energy* **2021**, *227*, 120333. [[CrossRef](#)]
22. Liu, J.Z.; Wang, Z.P.; Hou, Y.K.; Qu, C.H.; Hong, J.C.; Lin, N. Data-driven energy management and velocity prediction for four-wheel-independent-driving electric vehicles. *eTransportation* **2021**, *9*, 100119. [[CrossRef](#)]
23. Su, L.; Wu, M.; Li, Z.; Zhang, J. Cycle life prediction of lithium-ion batteries based on data-driven methods. *eTransportation* **2021**, *10*, 100137. [[CrossRef](#)]
24. Waag, W.; Fleischer, C.; Sauer, D.U. Critical review of the methods for monitoring of lithium-ion batteries in electric and hybrid vehicles. *J. Power Sources* **2014**, *258*, 321–339. [[CrossRef](#)]
25. Zheng, Y.; Qin, C.; Lai, X.; Han, X.; Xie, Y. A novel capacity estimation method for lithium-ion batteries using fusion estimation of charging curve sections and discrete Arrhenius aging model. *Appl. Energy* **2019**, *251*, 113327. [[CrossRef](#)]
26. Li, K.; Zhou, P.; Lu, Y.; Han, X.; Li, X.; Zheng, Y. Battery life estimation based on cloud data for electric vehicles. *J. Power Sources* **2020**, *468*, 228192. [[CrossRef](#)]
27. Khalid, A.; Sarwat, A.I. Fast Charging Li-Ion Battery Capacity Fade Prognostic Modeling Using Correlated Parameters’ Decomposition and Recurrent Wavelet Neural Network. In Proceedings of the IEEE Transportation Electrification Conference and Expo (ITEC), Electr Network, Chicago, IL, USA, 21–25 June 2021; pp. 27–32.
28. Davies, J.; Kurani, K.S. Moving from assumption to observation: Implications for energy and emissions impacts of plug-in hybrid electric vehicles. *Energy Policy* **2013**, *62*, 550–560. [[CrossRef](#)]
29. Duhon, A.N.; Sevel, K.S.; Tarnowsky, S.A.; Savagian, P.J. Chevrolet volt electric utilization. *SAE Int. J. Altern. Powertrains* **2015**, *4*, 269–276. [[CrossRef](#)]
30. Kelly, J.C.; MacDonald, J.S.; Keoleian, G.A. Time-dependent plug-in hybrid electric vehicle charging based on national driving patterns and demographics. *Appl. Energy* **2012**, *94*, 395–405. [[CrossRef](#)]
31. Goebel, D.; Plotz, P. Machine learning estimates of plug-in hybrid electric vehicle utility factors. *Transp. Res. Part D-Transp. Environ.* **2019**, *72*, 36–46. [[CrossRef](#)]
32. GB/T 32960.3-2016; Technical Specifications of Eemote Service and Management System for Electric Vehicles—Part 3: Communication Protocol and Data Format. National Standard of the People’s Republic of China: Beijing, China, 2016.
33. Duoba, M. Developing a utility factor for battery electric vehicles. *SAE Int. J. Altern. Powertrains* **2013**, *2*, 362–368. [[CrossRef](#)]
34. Zheng, Y.J.; Cui, Y.F.; Han, X.B.; Ouyang, M.G. A capacity prediction framework for lithium-ion batteries using fusion prediction of empirical model and data-driven method. *Energy* **2021**, *237*, 121556. [[CrossRef](#)]
35. Han, X. Study on Li-ion Battery Mechanism Model and State Estimation for Electric Vehicles. Ph.D. Thesis, Tsinghua University, Beijing, China, 2014.

Disclaimer/Publisher’s Note: The statements, opinions and data contained in all publications are solely those of the individual author(s) and contributor(s) and not of MDPI and/or the editor(s). MDPI and/or the editor(s) disclaim responsibility for any injury to people or property resulting from any ideas, methods, instructions or products referred to in the content.